ACS APPLIED MATERIALS & INTERFACES

Research Article

www.acsami.org

Fabrication of Well-Ordered Three-Phase Boundary with Nanostructure Pore Array for Mixed Potential-Type Zirconia-Based NO_2 Sensor

Bin Wang,[‡] Fangmeng Liu,[‡] Xue Yang,[‡] Yehui Guan,[‡] Ce Ma,[‡] Xidong Hao,[‡] Xishuang Liang,*[,†,‡] Fengmin Liu,[‡] Peng Sun,[‡] Tong Zhang,[‡] and Geyu Lu*[,†,‡]

[†]State Key Laboratory of Automotive Simulation and Control, Jilin University, 5988 Renmin Avenue, Changchun, Jilin 130012, China

[‡]State Key Laboratory on Integrated Optoelectronics, College of Electronic Science and Engineering, Jilin University, 2699 Qianjin Street, Changchun, Jilin 130012, China

ABSTRACT: A well-ordered porous three-phase boundary (TPB) was prepared with a polystyrene sphere as template and examined to improve the sensitivity of yttria-stabilized zirconia (YSZ)-based mixed-potential-type NO_2 sensor due to the increase of the electrochemical reaction active sites. The shape of pore array on the YSZ substrate surface can be controlled through changing the concentration of the precursor solution (Zr^{4+}/Y^{3+} = 23 mol/L/4 mol/L) and treatment conditions. An ordered hemispherical array was obtained when C_{Zr}^{4+} = 0.2 mol/L. The processed YSZ substrates were used to fabricate the sensors, and different sensitivities caused by different morphologies were tested. The sensor with well-ordered porous TPB exhibited the highest sensitivity to NO_2 with a response value of 105 mV to 100 ppm of NO_2, which is approximately twice as much as the smooth one. In addition, the sensor also showed good stability and speedy response kinetics. All these enhanced sensing properties might be due to the structure and morphology of the enlarged TPB.

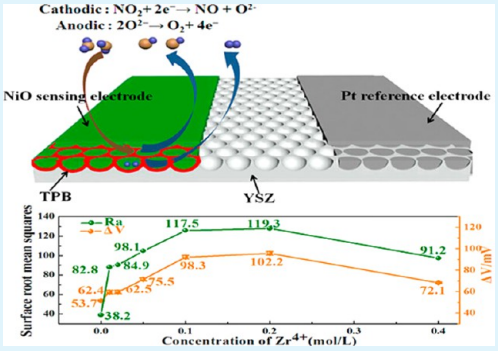

KEYWORDS: *YSZ, PSs template, ordered pore array, NO_2 sensor, three-phase boundary*

INTRODUCTION

Yttria-stabilized zirconia (YSZ)-based NO_x sensor is one of the most advantageous devices[1−5] because of its high operation temperature and mechanical and chemical stability. The sensor has been extensively applied in monitoring the automotive vehicle exhaust. Electrode materials and the structure of the three-phase boundary (TPB) were two main factors affecting the sensing properties of the sensor. Miura et al. fabricated the mixed-potential type NO_2 sensor, which used NiO as sensing electrode material and has excellent sensitivity to NO_2 at high temperature.[6,7] Recently, the effect of the microstructure of TPB had drawn considerable attention. The enlarged effective area of the TPB may extend the electrochemical reaction active sites and improves the sensing performance of the sensor. For example, our group used hydrofluoric acid corrosion and sand blasting technology to enlarge the surface area of YSZ substrate.[8,9] All the aforementioned methods significantly improve the response value of the sensor to NO_2. However, constructing the same structure in every experiment was difficult, and our group also developed femtosecond laser direct writing technology to control the surface morphology of the YSZ substrate.[10] By using this method, a micrometer-range ordered structure was successfully constructed. However, the femtosecond laser direct writing system was too expensive. Thus, developing a simple and inexpensive way to fabricate the TPB with controllable morphology is becoming more essential.

The self-assembly technique combined with the solution-dipping strategy is a cost-effective and simple way to create micrometer-scale pore array.[11,12] The combination of the self-assembled polystyrene sphere (PSs) template method and solution-dipping strategy was an efficient approach to create periodic nanostructures. In addition, structures, such as nanobowl,[13−17] nanorod,[18] nanohoneycomb,[19] and nanoring arrays,[20−22] as well as other nanostructures,[23−27] have been fabricated. After the self-assembly process, the PSs come into the monolayer template; then, PSs template is transferred to the precursor solution, and the template will float due to the surface tension of the solution. After the solution-dipping process, the template is picked by the substrate. After heat treatment, the PSs template is removed and the ordered pore array is eventually formed. To date, many studies on ordinary glass or silicon substrates[28] have been conducted using the aforementioned methods. However, only a few studies on YSZ substrate have been conducted.

In this study, PSs colloidal monolayer was used as a template, combined with the solution-dipping template strategy and self-assembly technology, to fabricate well-ordered nanostructured porous YSZ film on the YSZ substrate. Then, a high-

Received: April 10, 2016
Accepted: June 13, 2016
Published: June 13, 2016

DOI: 10.1021/acsami.6b04219
ACS Appl. Mater. Interfaces 2016, 8, 16752−16760

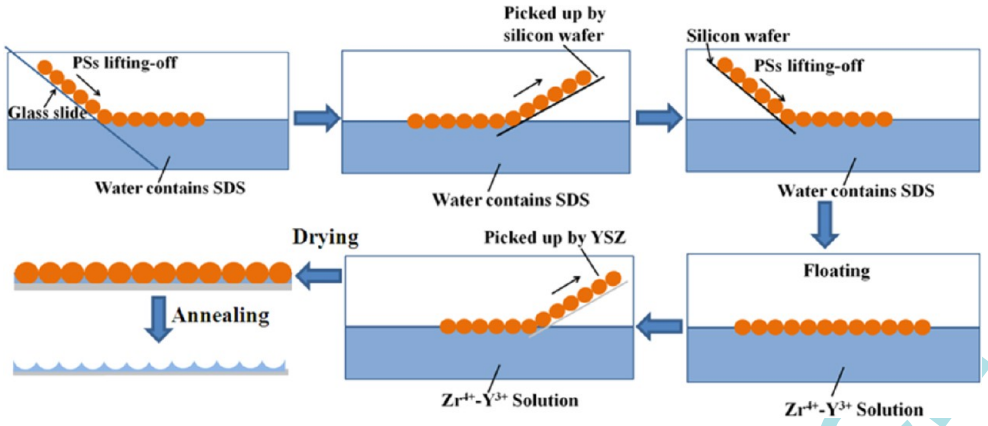

Figure 1. Flowchart of the fabrication strategy for the YSZ nanostructured pore array film.

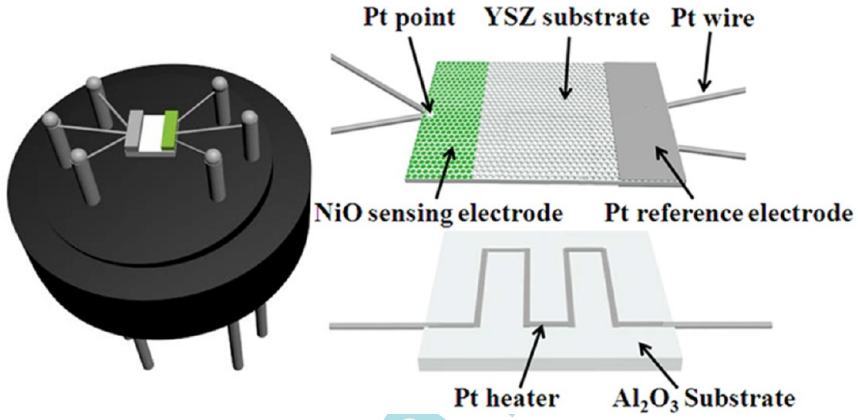

Figure 2. Schematic diagram of the sensor.

performance YSZ-based NO_2 sensor, which used NiO as sensing electrode and YSZ substrate with pore array as electrolyte, was fabricated and measured.

EXPERIMENTAL SECTION

Preparation of Well-Ordered YSZ Nanostructured Pore Arrays. The solution-dipping template synthesis strategy is shown in Figure 1. First, the glass slide and silicon wafer were cleaned in a mixed solution of 30%H_2O_2 and H_2SO_4 at 100 °C for about 1 h to prepare a hydroxylated surface. Once cooled, the cleaned glass slide was placed at the edge of the culture dish, which contained deionized water and sodium dodecyl sulfate (SDS; 10 wt %; H_2O/SDS = 100 mL/35 μL). Then, the PSs (provided by Alfa Aesar) suspension (PSs/deionized water/ethanol = 0.1 g/1 mL/1 mL) was lifted off from the glass slide. PSs would float on the solution due to the surface tension. After the self-assembly process, PSs would come into the monolayer PSs template, and the cleaned silicon wafer was used to pick up the PSs colloidal crystal template. Then, the PSs colloidal crystal template was slowly immersed into the precursor solution (C_{Zr}^{4+} = 0.01, 0.02, 0.05, 0.1, 0.2, and 0.4 mol/L), keeping the same molar ratio of the YSZ substrate (8% YSZ, provided by Anpeisheng Corp., China, Y_2O_3/ZrO_2= 0.08/0.92). Due to the surface tension and the difference of wettability between PSs and the silicon wafer, the PSs could be detached from the substrate and float on the precursor solution surface. After a 2 h solution-dipping process, the precursor solution was fully filled into the interstitial spaces between PS spheres. Then YSZ substrate was used to pick up the floating colloidal monolayer. The flat surface of the YSZ substrate was covered by the colloidal monolayer template, and the precursor solution fully filled in the interstitial spaces between the substrate and PSs template. Then, the YSZ substrate covered with PSs template was annealed at 1000 °C. The PSs were removed after a 1 h heat-treatment; the solute (Y_2O_3, ZrO_2) was gradually deposited onto the surface of YSZ substrate, and the YSZ substrates with an ordered nanostructure pore array film were obtained. The film and the YSZ substrate were firmly combined because pore array film was directly grown on the surface of YSZ at 1000 °C.[29−32]

Fabrication and Measurement of the Sensor. Planar-type NO_2 sensors were fabricated using the unprocessed and processed YSZ substrate after different concentrations of solution dipping (C_{Zr}^{4+} = 0.01, 0.02, 0.05, 0.1, 0.2, and 0.4 mol/L), which were labeled as S0, S1, S2, S3, S4, S5, and S6. The chemical precipitation method was used for synthesis of NiO, and the precursor of NiO ($Ni(OH)_2$) was sintered at 1100 °C for bout 3 h; NiO material was obtained.[33−35]The stripe-shaped Pt (0.5 mm × 2 mm) acted as the reference electrode (RE), and the sensing electrode (SE) was fabricated through the point-shaped Pt (0.8 mm × 2 mm) covered by the NiO layer. The devices were sintered at 800 °C for 3 h. A schematic diagram is shown in Figure 2.

The phase structure of SE material (NiO) was characterized through XRD patterns on a Rigaku wide-angle X-ray diffractometer (wavelength = 0.1541 nm). The morphology and the nanostructure of YSZ substrate were investigated by field emission scanning electron microscopy (SEM) using a JEOL JSM-7500F microscope with an accelerating voltage of 15 kV and atomic force microscope (AFM; Being Nano-Instrument, Ltd., CSPM5500, China). The response signal (V) of the sensor to measured gas was tested using a digital electrometer (Rigol DM3054) connected to a computer. The polarization curves of sensor S0 and S5 in air or sample gas (50 and 100 ppm of NO_2 + air) were measured by using an electrochemical workstation (CHI600C, Instrument Corporation of Shanghai, China).

DOI: 10.1021/acsami.6b04219
ACS Appl. Mater. Interfaces 2016, 8, 16752−16760

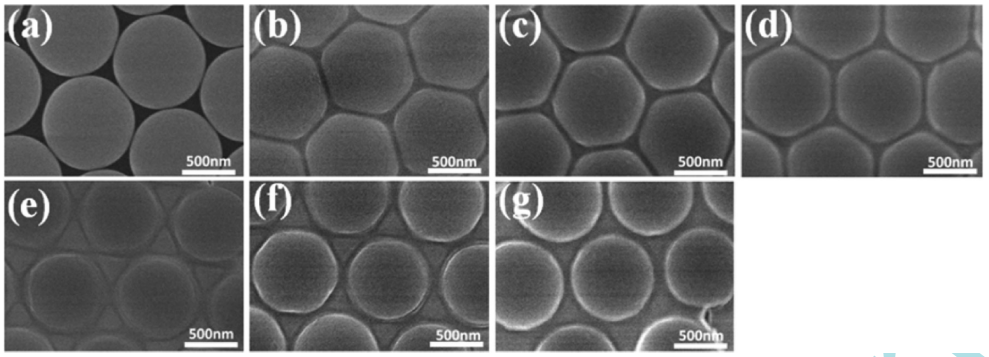

Figure 3. PS spheres template before (a) and after dipping with different concentrations of precursor solution: (b) C_{Zr}^{4+} = 0.01 mol/L; (c) C_{Zr}^{4+} = 0.02 mol/L; (d) C_{Zr}^{4+} = 0.05 mol/L; (e) C_{Zr}^{4+} = 0.1 mol/L; (f) C_{Zr}^{4+} = 0.2 mol/L; (g) C_{Zr}^{4+} = 0.4 mol/L.

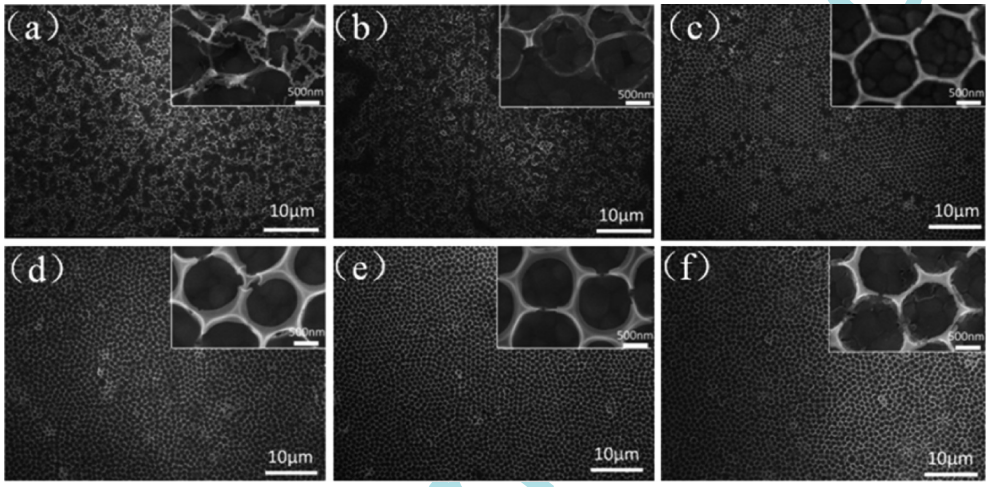

Figure 4. Morphological and microstructured characterizations of the YSZ nanostructure pore array thin films sintered at 1000 °C. (a) C_{Zr}^{4+} = 0.01 mol/L, (b) C_{Zr}^{4+} = 0.02 mol/L, (c) C_{Zr}^{4+} = 0.05 mol/L, (d) C_{Zr}^{4+} = 0.1 mol/L, (e) C_{Zr}^{4+} = 0.2 mol/L, and (f) C_{Zr}^{4+} = 0.4 mol/L.

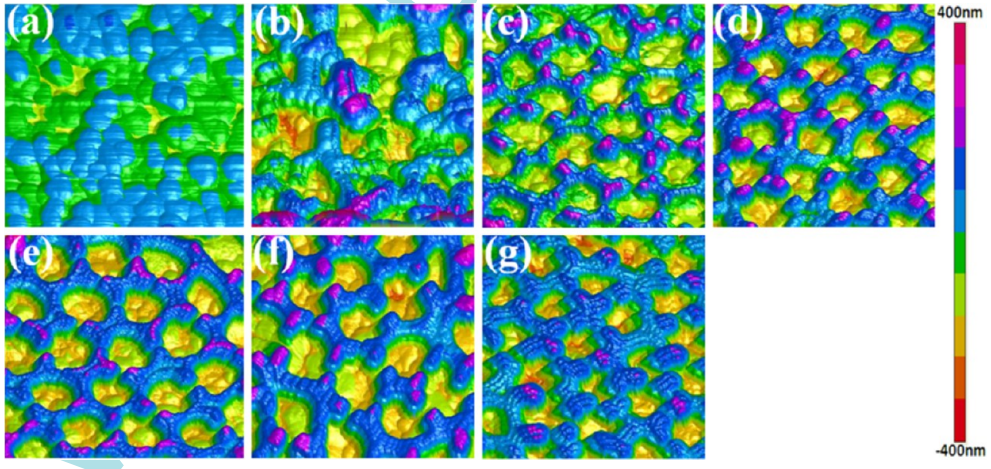

Figure 5. AFM images of (a) smooth YSZ and the YSZ ordered thin films after annealing at 1000 °C with (b) C_{Zr}^{4+} = 0.01 mol/L; (c) C_{Zr}^{4+} = 0.02 mol/L; (d) C_{Zr}^{4+} = 0.05 mol/L; (e) C_{Zr}^{4+} = 0.1 mol/L; (f) C_{Zr}^{4+} = 0.2 mol/L; (g) C_{Zr}^{4+} = 0.4 mol/L.

RESULTS AND DISCUSSION

Fabrication of Nanostructure Pore Array Films. In this experiment, after the self-assembly process, the ordered PSs template was obtained, as indicated in Figure 3a. PS spheres still keep the shape and take on the most closely packed arrangement. After the self-assembly process, monolayer colloidal crystals were transferred to different concentration precursors for solution dipping for approximately 2 h. Their morphologies were different, as shown in Figure 3b–g. Compared with the colloidal monolayer without solution dipping (Figure 3a), the deformation caused by a higher concentration of dipping solution leads to a change from facet contact (Figure 3b–d) to quasi-point contact (Figure 3e–g) between neighboring PSs. Correspondingly, the interstices between PS spheres become wider and wider. The shape of the PSs changed due to the different buoyancy forces caused by the

DOI: 10.1021/acsami.6b04219
ACS Appl. Mater. Interfaces 2016, 8, 16752–16760

Table 1. Comparison of the Depth, Width, and Ra of the Nanostructure

concentration (mol/L)	0	0.01	0.02	0.05	0.1	0.2	0.4
depth (nm)	0	275	300	350	350	350	350
width (nm)	0	750	800	950	980	980	920
Ra	38.2	82.8	84.9	98.1	117.5	119.3	91.2

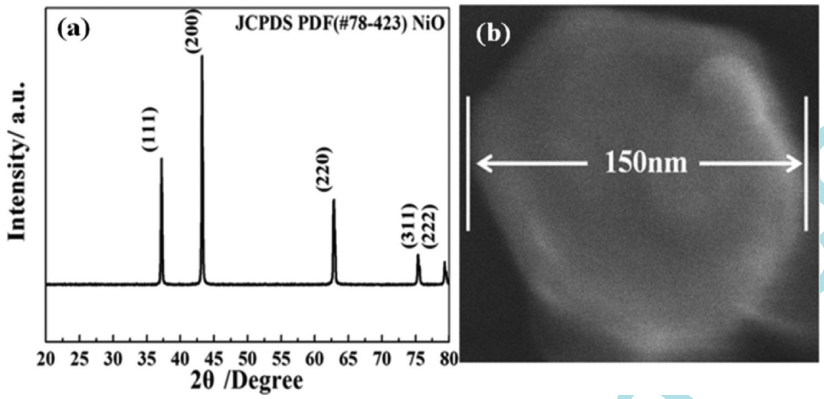

Figure 6. (a) XRD pattern and (b) SEM image of NiO.

different concentration precursors. When the concentration was low (C_{Zr}^{4+} = 0.01 and 0.02 mol/L), the buoyancy force was small. This condition is conducive for PSs to come in contact and huddle together with the YSZ surface. When the solution concentration was higher (C_{Zr}^{4+} = 0.2 and 0.4 mol/L), the buoyancy force also increased, resulting in a decrease in pressure between the two PSs. Obviously, the shape of the PSs can be well-tuned by controlling the concentration of the solution-dipping template.[36−38]

Figure 4 shows the SEM images of prepared YSZ nanostructure films using PSs monolayer template with different concentrations of solution dipping. When the precursor concentration is at a lower level (C_{Zr}^{4+} = 0.01 and 0.02 mol/L), the structure is unordered and weak. When the precursor concentration increased from C_{Zr}^{4+}= 0.05 mol/L to C_{Zr}^{4+} = 0.2 mol/L, an ordered nanostructure pore array film was successfully fabricated on the YSZ substrate surface, and its shape is determined by the concentration of the solution. The shape of the YSZ nanostructure thin film changed from hexagon to circular with the increase of precursor concentration, as shown in Figure 4c−e. The nanostructure pore arrays were badly destroyed and became irregular at higher concentration (C_{Zr}^{4+} = 0.4 mol/L). At the same time, a lot of nanogaps were generated on the walls between two neighboring nanostructure pores (Figure 4f).

In order to show the change of the nanostructure more clearly, AFM was also used to illustrate the morphology of the YSZ substrate surface, as shown in Figure 5. With the increase in precursor concentration, the thickness of nanostructure pore array films will correspondingly increase. The width of the nanostructure increased from 750 to 980 nm, when C_{Zr}^{4+} changed in the range of 0.01 to 0.2 mol/L. However, at a higher concentration (C_{Zr}^{4+} = 0.4 mol/L), the width decreases to 920 nm. The depth of the nanostructure increases from 275 to 350 nm with the increase in precursor concentration in the range of 0.01 to 0.05 mol/L. When the precursor concentration is higher (C_{Zr}^{4+} = 0.05 to 0.4 mol/L), the depth of the nanostructure remains at 350 nm. In general, when the nanostructure pore array film was annealed, thermal stress will be generated on the film surface. The influence of thermal stress on the morphology of the nanostructure pore array film is becoming more serious with the increase in film thickness. With the increase in precursor concentration, the thickness of the nanostructure pore array film increases with the increase of the concentration of the dipping solution. When precursor concentration was relatively small (C_{Zr}^{4+} = 0.05, 0.1 mol/L), the thermal stress had a weak effect on nanostructure pore array films in the heat-treatment at 1000 °C for 1 h. Therefore, the nanostructure array film on the YSZ substrate is in the same shape as the PSs template after solution dipping and displays a regular pore. However, when the precursor concentration was increased (C_{Zr}^{4+} = 0.1, 0.2 mol/L), the thickness between neighboring nanostructures correspondingly increased. With the increase in thermal stress on the film surface, a lot of nanogaps were generated on the walls between two neighboring nanostructures. When the thickness of the nanostructure was increased further by the increase in precursor concentration (C_{Zr}^{4+} = 0.4 mol/L), the influence of thermal stress becomes more significant, and the nanostructure pore array was out of shape due to the influence of serious thermal stress. The surface root mean squares (Ra) obtained from AFM images were used to show the roughness of the YSZ substrate surface, and the corresponding result was shown in Table 1. When the precursor concentration is in the range of 0−0.2 mol/L, Ra increases from 38.2 to 119.3. When the precursor concentration was higher, the value of Ra decreases to 91.2. Taking the integrity and specific dimension into account, C_{Zr}^{4+} = 0.2 mol/L was considered to be the best concentration to construct the ordered nanostructure pore array.

The XRD pattern of the as-synthesized product though the precipitation method is shown in Figure 6a. The pattern is consistent with JCPDS File No.78-423, and the phase of synthesized NiO is a suitably crystalline cubic structure. As shown in Figure 6b, the diameter of the NiO nanoparticle is about 150 nm, and the size of the formed nanostructure is in the range of 750−980 nm. Thus, abundant NiO sensing particles can be easily incorporated into ordered nanostructure and provide a larger contact area between NiO SE material and electrolyte to enlarge the TPB area. The active sites of

DOI: 10.1021/acsami.6b04219
ACS Appl. Mater. Interfaces 2016, 8, 16752−16760

electrochemical reactions were increased, and the reaction rate was also improved because of the enlarged TPB area.

Sensing Performances of the NO_2 Sensors. The response of the YSZ-based gas sensor highly relies on the operating temperature.[39,40] Thus, the best operating temperature of sensor S5 was investigated first (S5: sensor with the processed YSZ substrate which was covered with the best integrity ordered nanostructure pore array film). The response and recovery properties of sensor S5 at different operating temperatures are exhibited in Figure 7. The response value

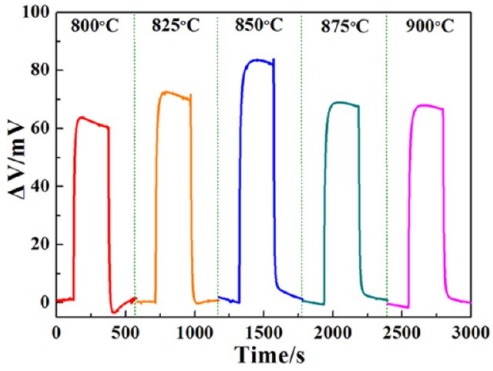

Figure 7. Responses of sensor S5 to 50 ppm of NO_2 at different temperatures.

tends to increase with the initial increase in temperature, and the value for maximum response to 50 ppm of NO_2 was obtained at 850 °C. At a higher temperature, the response to 50 ppm of NO_2 tended to decrease. The reason for this phenomenon is that the electrochemical reactions occurring at the TPB need a certain active energy below 850 °C. As temperatures rise, the sensitivity of the sensor will improve below 850 °C. However, when the temperature was higher than 850 °C, a lot of nitrogen dioxide molecule desorb from the sensing electrode with the increase in temperature. Thus, the response of the sensor decreased due to a temperature further increase. Consequently, 850 °C was considered as the best operating temperature and was used in the subsequent sensitivity property tests.

Figure 8a shows the response and recovery performances of S0, S1, S2, S3, S4, S5, and S6 to different concentrations of NO_2. The response of sensor S5 to 100 ppm of NO_2 was 105 mV, approximately twice as much as sensor S0. The response increased with the improvement in the integrity of the nanostructure. For the sensors S0 and S5, the dependences of ΔV on NO_2 concentrations are investigated and shown in Figure 8b. The ΔV values were almost linear with the logarithm of the NO_2 concentration in the range of 10−400 ppm at 850 °C. The slope of sensor S5 was approximately 53.9 mV/decade, whereas sensor S0 was approximately 30.3 mV/decade. This result clearly showed that the YSZ nanostructure pore films could effectively enhance the sensitivity.

In order to explain the enhancement of the sensitivity, the mechanism of the mixed potential type gas sensor was discussed first. Apparently, when the sensor is exposed to the NO_2 atmosphere, a local cell is formed due to the cathodic $NO_2 + 2e^- \rightarrow NO + O^{2-}$ (1) and anodic $2O^{2-} \rightarrow O_2 + 4e^-$ (2) reactions taking place at the TPB of the sensing electrode. When the reaction rate of the cathodic reaction is equal to the anodic reaction, the mixed potential is generated, as shown in Figure 9. TPB provides the reaction field for reactions (1) and (2); a higher roughness value means a larger interface between NiO and the YSZ substrate, which could provide more active sites for the electrochemical reactions.[41,42] As indicated in Figure 10, Ra increased from 38.2 to 119.3 and the response of S0−S5 to 100 ppm of NO_2 also increased from 53.7 to 102.2 mV. The sensors S4 and S5 generate almost the same NO_2 sensitivity with nearly the same roughness value. Moreover, compared to S5, the sensor S6 has a lower roughness value, which means a relatively small number of electrochemical reaction active sites. Thus, the sensor S6 generated lower NO_2 sensitivity than S5. Obviously, as showed in Figure 10, the response value of S0−S6 to 100 ppm of NO_2 was in accordance with the variation curve of Ra, and the correlation coefficients of two curves is 0.89, which showed a strong pertinent relation.

Sensor S5 has the highest response to 10−400 ppm of NO_2 and processed the perfect YSZ nanostructure porous array film on the YSZ substrate. Figure 11a illustrated the response transients to 50 ppm of NO_2 repeated 9 times at 850 °C. The ΔV of each time was almost equal, and the sensor exhibited good repeatability. Cross-sensitivities for sensor S5 to 100 ppm of various gases, such as C_2H_4, H_2, CH_4, and CO mixed with 100 ppm of NO_2 at 850 °C, were tested, and the result is shown in Figure 11b. Compared with 100 ppm of pure NO_2, the response of the sensor S5 to mixed gases slightly decreased. It demonstrated that the sensor S5 has relative good selectivity to NO_2 in the mixed gas atmosphere. In addition, the 30 day long-term stability of sensor S5 was tested. The result is shown in Figure 11c. The ΔV_s ($\Delta V_s = [(\Delta V_n - \Delta V_0)/\Delta V_0 \times 100\%]$, where ΔV_0 and ΔV_n represent the ΔV of the sensor in the 0

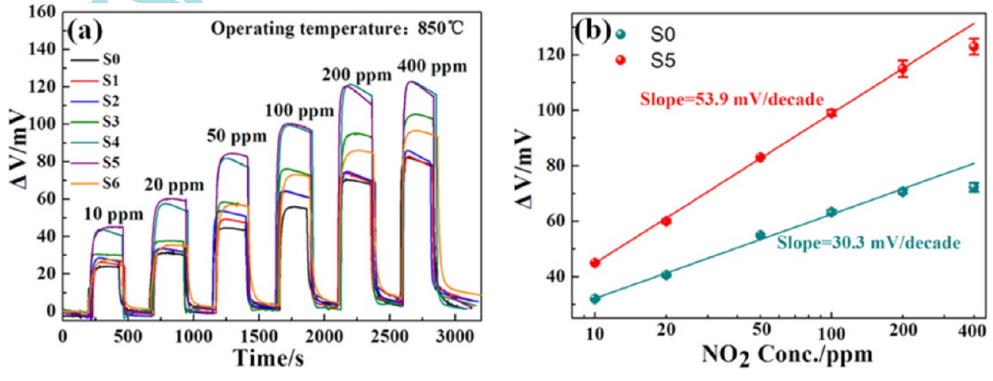

Figure 8. (a) Response transients of the different sensors to various NO_2 concentrations in the range of 10−400 ppm at 850 °C. (b) The dependence of the ΔV on the logarithm of NO_2 concentrations for S0 and S5.

DOI: 10.1021/acsami.6b04219
ACS Appl. Mater. Interfaces 2016, 8, 16752−16760

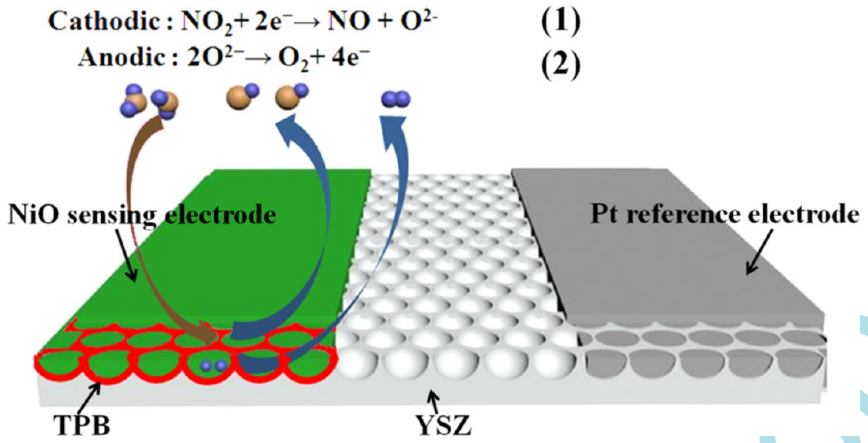

Figure 9. Schematic representation of the NO_2 sensing mechanism for the fabricated sensor.

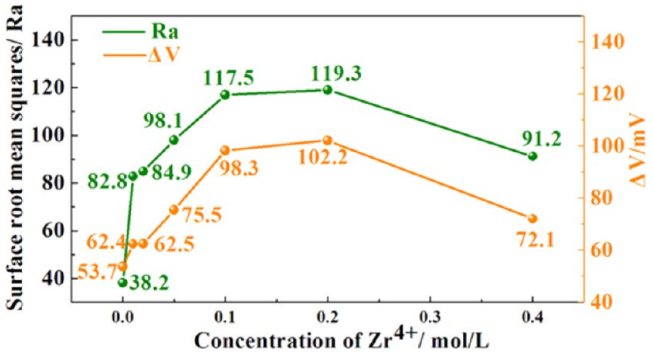

Figure 10. Variation curve of Ra and the response of different sensors to 100 ppm of NO_2.

and *n*th day) was used to show the change in degree of ΔV with time. In the figure, sensor S5 maintained a good response to 50 and 100 ppm of NO_2 within ±4% charge, which exhibits good stability.

As for the detection of a certain concentration of NO_2, the mixed potential is linear with the logarithm of O_2 and the slope was negative; the above phenomena coincided with the mixed-potential sensing model.[43,44] The effect of the coexisting oxygen transient of sensor S5 to 50 ppm of NO_2 was investigated to verify this conclusion. The result is shown in Figure 12. The potential difference was almost linear to the logarithm of the O_2 concentration, which shows a minus slope. Such a result could clearly examine the sensing mechanism involved in the mixed potential.

In order to explain the reason for the enhancement of sensitivity, the polarization curves of the sensor S0 and S5 in

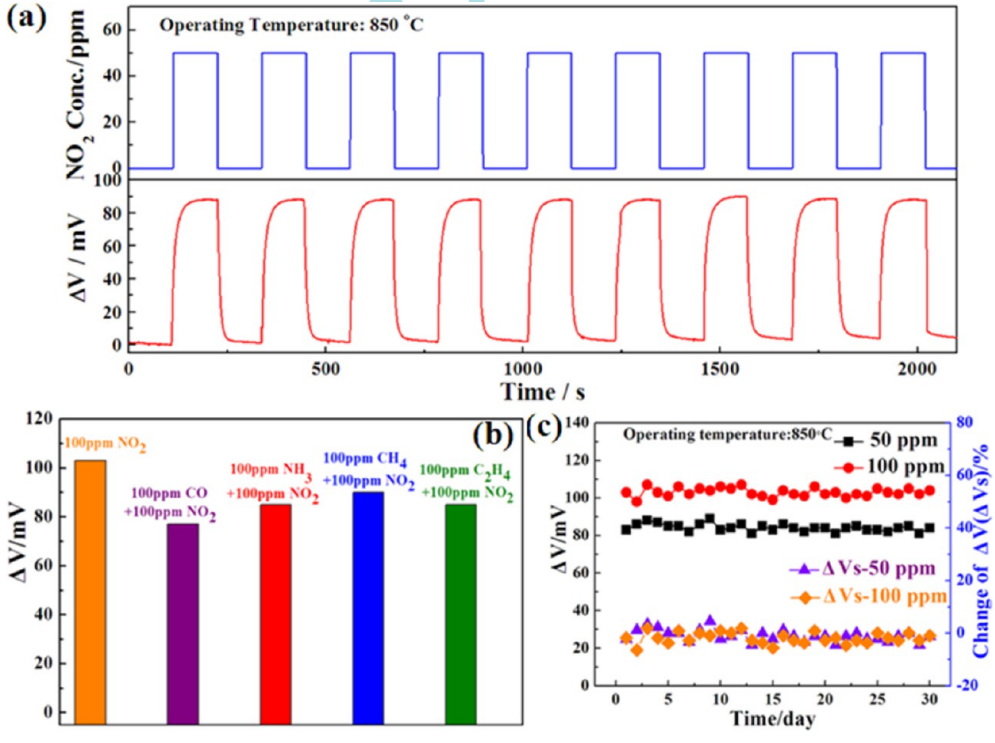

Figure 11. (a) Continuous response and recovery transients of sensor S5 to 50 ppm of NO_2 at 850 °C. (b) Cross-sensitivities to various gases for sensor S5 at 850 °C. (c) Time dependence of the ΔV to 50 and 100 ppm of NO_2.

DOI: 10.1021/acsami.6b04219
ACS Appl. Mater. Interfaces 2016, 8, 16752−16760

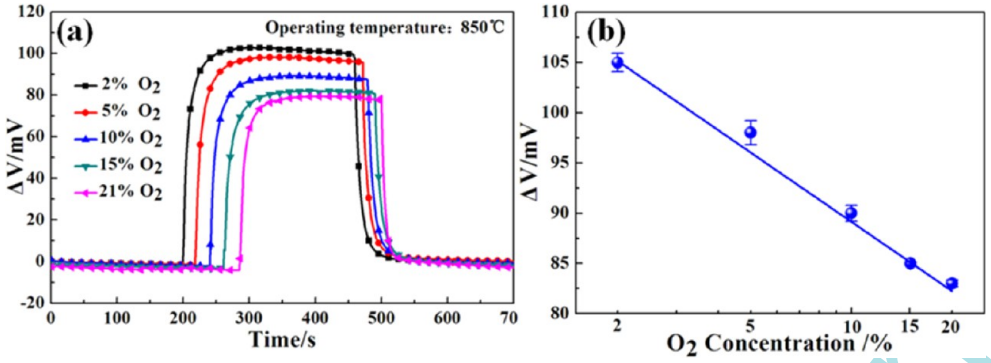

Figure 12. (a) Responses of sensor S5 to 50 ppm of NO_2 at different concentrations of O_2 at 850 °C and (b) dependence of the ΔV on the logarithm of O_2 concentrations.

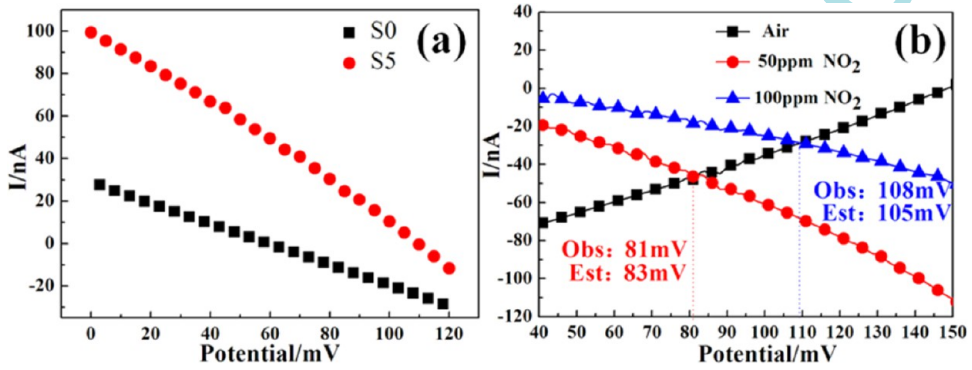

Figure 13. (a) Polarization curves of sensor S0 and S5 in 100 ppm of NO_2 (+air) and (b) modified polarization curves of sensor S5 to air, 50 and 100 ppm of NO_2 at 850 °C.

100 ppm of NO_2 (+air) were measured as shown in Figure 13a. Compared with the polarization curve of sensor S0 in 100 ppm of NO_2 (+air), the polarization curve of S5 tends to shift upward. This shift in the polarization curve is due to a more intense cathodic reaction (1), which could enhance the sensitivity. Besides, for validating the mixed-potential mechanism, the modified polarization curves of the sensor S5 in air, 50 and 100 ppm of NO_2 for the sensor S5, were measured and exhibited in Figure 13b. The cathodic polarization curve was obtained by subtracting in air from NO_2 + air, and the anodic polarization curve was obtained in air. The intersection of the anodic and cathodic polarization curves is the theoretical value of mixed potential. Obviously, the experimental potential difference values were almost equal to the estimated values. Thus, the correctness of mixed-potential theory was verified by the aforementioned experimental evaluation.

CONCLUSION

In this work, the well-ordered YSZ nanostructure pore array films on the surface of the YSZ substrate were formed successfully using the solution dipping PSs template method. The concentration of the precursor solution (Zr^{4+}/Y^{3+} = 23 mol/L/4 mol/L) could highly influence the shape of the nanostructure pore array film. The mixed-potential type electrochemical NO_2 sensors based on processed YSZ with three-dimension three-phase boundary and NiO-SE were fabricated, and sensing characteristics were investigated at elevated temperature. The response value of the sensor with nanostructure pore array films to 10−400 ppm of NO_2 exhibited significant improvements at 850 °C compared with that of unprocessed. The sensor S5 has the most perfect nanostructure pore array film on YSZ substrate, and the sensitivity to NO_2 was as high as 53.9 mV/decade. This result could be explained by the larger area of the TPB. Meanwhile, the sensor S5 also had good repeatability, selectivity, and stability to NO_2.

AUTHOR INFORMATION

Corresponding Authors

*Phone: +86 431 85168384. Fax: +86 431 85167808. E-mail: liangxs@jlu.edu.cn (X.L.).

*Phone: +86 431 85168384. Fax: +86 431 85167808. E-mail: lugy@jlu.edu.cn (G.L.).

Notes

The authors declare no competing financial interest.

ACKNOWLEDGMENTS

This work is supported by the National Nature Science Foundation of China (Nos. 61327804, 61473132, 61520106003, 61134010, 61374218, and 61533021) Program for Chang Jiang Scholars and Innovative Research Team in University (No. IRT13018) and National High-Tech Research and Development Program of China (863 Program No. 2014AA06A505), Application and Basic Research of Jilin Province (2013010 2010JC).

ABBREVIATIONS

XRD = X-ray diffraction
FESEM = field-emission electron scanning microscopy
AFM = atomic force microscope
YSZ = yttria-stabilized zirconia

DOI: 10.1021/acsami.6b04219
ACS Appl. Mater. Interfaces 2016, 8, 16752−16760

TPB = three-phase boundary
PSs = polystyrene sphere
RE = reference electrode
SE = sensing electrode

REFERENCES

(1) Miura, N.; Lu, G. Y.; Yamazoe, N. High-Temperature Potentiometric: Amperometric NO_x Sensors. *Sens. Actuators, B* **1998**, *52*, 169−178.
(2) Zhuiykov, S.; Miura, N. Development of Zirconia-Based Potentiometric NO_x Sensors for Automotive and Energy Industries in the Early 21st Century: What Are the Prospects for Sensors? *Sens. Actuators, B* **2007**, *121*, 639−651.
(3) Lu, G. Y.; Miura, N.; Yamazoe, N. High-Temperature Sensors for NO and NO_2 Based on Stabilized Zirconia and Spinel-Type Oxide Electrodes. *J. Mater. Chem.* **1997**, *7*, 1445−1449.
(4) Dai, L.; Yang, G. X.; Zhou, H. Z.; He, Z. X.; Li, Y. H.; Wang, L. Mixed Potential NH_3 Sensor Based on Mg-doped lanthanum silicate oxyapatite. *Sens. Actuators, B* **2016**, *224*, 356−363.
(5) Li, X. D.; Wang, C.; Wang, B.; Yuan, Y.; Huang, J. Q.; Zhang, H. B.; Xia, F.; Xiao, J. Z. Effects of Sintering Temperature on the NH_3 Sensing Properties of $Mg_2Cu_{0.25}Fe_1O_{3.75}$ Electrode for YSZ-Based Potentiometric NH_3 Sensor. *Ceram. Int.* **2016**, *42*, 2214−2220.
(6) Miura, N.; Wang, J.; Nakatou, M.; Elumalai, P.; Zhuiykov, S.; Hasei, M. High-Temperature Operating Characteristics of Mixed-Potential-Type NO_2 Sensor Based on Stabilized-Zirconia Tube and NiO Sensing Electrode. *Sens. Actuators, B* **2006**, *114*, 903−909.
(7) Miura, N.; Sato, T.; Anggraini, A. S.; Ikeda, H.; Zhuiykov, S. A Review of Mixed-Potential Type Zirconia-Based Gas Sensors. *Ionics* **2014**, *20*, 901−925.
(8) Liang, X. S.; Yang, S. Q.; Li, J. G.; Zhang, H.; Diao, Q.; Zhao, W.; Lu, G. Y. Mixed-Potential-Type Zirconia-Based NO_2 Sensor with High-Performance Three-Phase Boundary. *Sens. Actuators, B* **2011**, *158*, 1−8.
(9) Sun, R. Z.; Guan, Y. H.; Cheng, X. Y.; Guan, Y. Z.; Liang, X. S.; Ma, J.; Sun, P.; Sun, Y. F.; Lu, G. Y. High Performance Three-Phase Boundary Obtained by Sand Blasting Technology for Mixed-Potential-Type Zirconia-Based NO_2 Sensors. *Sens. Actuators, B* **2015**, *210*, 91−95.
(10) Guan, Y. Z.; Li, C. H.; Cheng, X. Y.; Wang, B.; Sun, R. Z.; Liang, X. S.; Zhao, J. H.; Chen, H.; Lu, G. Y. Highly Sensitive Mixed-Potential-Type NO_2 Sensor With YSZ Processed Using Femtosecond Laser Direct Writing Technology. *Sens. Actuators, B* **2014**, *198*, 110−113.
(11) Li, Y.; Cai, W. P.; Cao, B. Q.; Duan, G. T.; Li, C. C.; Sun, F. Q.; Zeng, H. B. Morphology-Controlled 2D Ordered Arrays by Heating-Induced Deformation of 2D Colloidal Monolayer. *J. Mater. Chem.* **2006**, *16*, 609−612.
(12) Sun, F. Q.; Cai, W. P.; Li, Y.; Jia, L. C.; Lu, F. Direct Growth of Mono-and Multilayer Nanostructured Porous Films on Curved Surfaces and Their Application as Gas Sensors. *Adv. Mater.* **2005**, *17*, 2872−2877.
(13) Wang, X. D.; Graugnard, E.; King, J. S.; Wang, Z. L.; Summers, C. J. Large-Scale Fabrication of Ordered Nanobowl Arrays. *Nano Lett.* **2004**, *4*, 2223−2226.
(14) Wang, X. D.; Lao, C.; Graugnard, E.; Summers, C. J.; Wang, Z. L. Large-Size Liftable Inverted-Nanobowl Sheets as Reusable Masks for Nanolithiography. *Nano Lett.* **2005**, *5*, 1784−1788.
(15) Li, Y.; Li, C. C.; Cho, S. O.; Duan, G. T.; Cai, W. P. Silver Hierarchical Bowl-Like Array: Synthesis, Superhydrophobicity, and Optical Properties. *Langmuir* **2007**, *23*, 9802−9807.
(16) Srivastava, A. K.; Madhavi, S.; White, T. J.; Ramanujan, R. V. Template Assisted Assembly of Cobalt Nanobowl Arrays. *J. Mater. Chem.* **2005**, *15*, 4424−4428.
(17) Chen, T. H.; Tsai, T. Y.; Hsieh, K. C.; Chang, S. C.; Tai, N. H.; Chen, H. L. Two-Dimensional Metallic Nanobowl Array Transferred onto Thermoplastic Substrates by Microwave Heating of Carbon Nanotubes. *Nanotechnology* **2008**, *19*, 465303.
(18) Wang, X. D.; Neff, C.; Graugnard, E.; Ding, Y.; King, J. S.; Pranger, L. A.; Tannenbaum, R.; Wang, Z. L.; Summers, C. J. Photonic Crystals Fabricated Using Patterned Nanorod Arrays. *Adv. Mater.* **2005**, *17*, 2103−2106.
(19) Kei, C. C.; Chen, T. H.; Chang, C. M.; Su, C. Y.; Lee, C. T.; Hsiao, C. N.; Chang, S. C.; Perng, T. P. Metal Oxide Nano-Honeycombs Prepared by Solution-Based Nanosphere Lithography and the Field Emission Properties. *Chem. Mater.* **2007**, *19*, 5833−5835.
(20) Kosiorek, A.; Kandulski, W.; Glaczynska, H.; Giersig, M. Fabrication of Nanoscale Rings, Dots, and Rods by Combining Shadow Nanosphere Lithography and Annealed Polystyrene Nanosphere Masks. *Small* **2005**, *1*, 439−444.
(21) Li, J. R.; Garno, J. C. Nanostructures of Octadecyltrisiloxane Self-Assembled Monolayers Produced on Au111 Using Particle Lithography. *ACS Appl. Mater. Interfaces* **2009**, *1*, 969−976.
(22) Sun, F. Q.; Yu, J. C.; Wang, X. C. Construction of Size-Controllable Hierarchical Nanoporous TiO_2 Ring Arrays and Their Modifications. *Chem. Mater.* **2006**, *18*, 3774−3779.
(23) Métraux, G. S.; Mirkin, C. A. Rapid Thermal Synthesis of Silver Nanoprisms with Chemically Tailorable Thickness. *Adv. Mater.* **2005**, *17*, 412−415.
(24) Sun, F.; Cai, W.; Li, Y.; Duan, G.; Nichols, W. T.; Liang, C.; Koshizaki, N.; Fang, Q.; Boyd, I. W. Laser Morphological Manipulation of Gold Nanoparticles Periodically Arranged on Solid Supports. *Appl. Phys. B: Lasers Opt.* **2005**, *81*, 765−768.
(25) Li, Y.; Cai, W. P.; Duan, G. T. Ordered Micro/Nanostructured Arrays Based on the Monolayer Colloidal Crystals. *Chem. Mater.* **2008**, *20*, 615−624.
(26) Trujillo, N. J.; Baxamusa, S. H.; Gleason, K. K. Grafted Polymeric Nanostructures Patterned Bottom−Up by Colloidal Lithography and Initiated Chemical Vapor Deposition (iCVD). *Chem. Mater.* **2009**, *21*, 742−750.
(27) Chen, X.; Wei, X.; Jiang, K. Fabrication of Large-Area Nickel Nanobump Arrays. *Microelectron. Eng.* **2009**, *86*, 871−873.
(28) Dai, Z. F.; Lee, C. S.; Kim, B. Y.; Kwak, C. H.; Yoon, J. W.; Jeong, H. M.; Lee, J. H. Honeycomb-like Periodic Porous $LaFeO_3$ Thin Film Chemiresistors with Enhanced Gas-Sensing Performances. *ACS Appl. Mater. Interfaces* **2014**, *6*, 16217−16226.
(29) Haynes, C. L.; Van Duyne, R. P. Nanosphere Lithography: A Versatile Nanofabrication Tool for Studies of Size-Dependent Nanoparticle Optics. *J. Phys. Chem. B* **2001**, *105*, 5599−5611.
(30) Cai, Z. Y.; Liu, Y. J.; Lu, X. M.; Teng, J. H. Fabrication of Well-Ordered Binary Colloidal Crystals with Extended Size Ratios for Broadband Reflectance. *ACS Appl. Mater. Interfaces* **2014**, *6*, 10265−10273.
(31) Yang, H. T.; Gozubenli, N.; Fang, Y.; Jiang, P. Generalized Fabrication of Monolayer Nonclose-Packed Colloidal Crystals with Tunable Lattice Spacing. *Langmuir* **2013**, *29*, 7674−7681.
(32) Li, Y.; Cai, W. P.; Cao, B. Q.; Duan, G. T.; Li, C. C.; Sun, F. Q.; Zeng, H. B. Morphology-Controlled 2D Ordered Arrays by Heating-Induced Deformation of 2D Colloidal Monolayer. *J. Mater. Chem.* **2006**, *16*, 609−612.
(33) Diao, Q.; Yin, C. G.; Liu, Y. W.; Li, J. G.; Gong, X.; Liang, X. S.; Yang, S. Q.; Chen, H.; Lu, G. Y. Mixed-Potential-Type NO_2 Sensor Using Stabilized Zirconia and Cr_2O_3−WO_3 Nanocomposites. *Sens. Actuators, B* **2013**, *180*, 90−95.
(34) Yin, C. G.; Guan, Y. Z.; Zhu, Z.; Liang, X. S.; Wang, B.; Diao, Q.; Zhang, H.; Ma, J.; Liu, F. M.; Sun, Y. F.; Zheng, J.; Lu, G. Y. Highly Sensitive Mixed-Potential-Type NO_2 Sensor Using Porous Double-Layer YSZ Substrate. *Sens. Actuators, B* **2013**, *183*, 474−477.
(35) Liu, F. M.; Guan, Y. H.; Sun, H. B.; Xu, X. M.; Sun, R. Z.; Liang, X. S.; Sun, P.; Gao, Y.; Lu, G. Y. YSZ-Based NO_2 Sensor Utilizing Hierarchical In_2O_3 Electrode. *Sens. Actuators, B* **2016**, *222*, 698−706.
(36) Xu, M. J.; Lu, N.; Qi, D. P.; Xu, H. B.; Wang, Y. D.; Shi, S. L.; Chi, L. F. Fabrication of Superhydrophobic Polymer Films with Hierarchical Silver Microbowl Array Structures. *J. Colloid Interface Sci.* **2011**, *360*, 300−304.

DOI: 10.1021/acsami.6b04219
ACS Appl. Mater. Interfaces 2016, 8, 16752−16760

(37) Weintraub, B.; Deng, Y. L.; Wang, Z. L. Position-Controlled Seedless Growth of ZnO Nanorod Arrays on a Polymer Substrate via Wet Chemical Synthesis. *J. Phys. Chem. C* **2007**, *111*, 10162−10165.
(38) Ye, X. Z.; Qi, L. M. Recent Advances in Fabrication of Monolayer Colloidal Crystals and Their Inverse Replicas. *Sci. China: Chem.* **2014**, *57*, 58−69.
(39) Lu, G. Y.; Miura, N.; Yamazoe, N. Stabilized Zirconia-Based Sensors Using WO_3 Electrode for Detection of NO or NO_2. *Sens. Actuators, B* **2000**, *65*, 125−127.
(40) Miura, N.; Lu, G. Y.; Yamazoe, N. High-Temperature Potentiometric: Amperometric NO_x Sensors Combining Stabilized Zirconia with Mixed-Metal Oxide Electrode. *Sens. Actuators, B* **1998**, *52*, 169−178.
(41) Liu, F. M.; Sun, R. Z.; Guan, Y. H.; Cheng, X. Y.; Zhang, H.; Guan, Y. Z.; Liang, X. S.; Sun, P.; Lu, G. Y. Mixed-Potential Type NH_3Sensor Based on Stabilized Zirconia and $Ni_3V_2O_8$ Sensing Electrode. *Sens. Actuators, B* **2015**, *210*, 795−802.
(42) Cheng, X. Y.; Wang, C.; Wang, B.; Sun, R. Z.; Guan, Y. Z.; Sun, Y. F.; Liang, X. S.; Sun, P.; Lu, G. Y. Mixed-Potential-Type YSZ-Based Sensor with Nano-Structured NiO and Porous TPB Processed with Pore-Formers Using Coating Technique. *Sens. Actuators, B* **2015**, *221*, 1321−1329.
(43) Miura, N.; Raisen, T.; Lu, G. Y.; Yamazoe, N. Highly Selective CO Sensor Using Stabilized Zirconia and A Couple of Oxide Electrodes. *Sens. Actuators, B* **1998**, *47*, 84−91.
(44) Miura, N.; Lu, G. Y.; Yamazoe, N. Progress in Mixed-Potential Type Devices Based on Solid Electrolyte for Sensing Redox Gases. *Solid State Ionics* **2000**, *136-137*, 533−542.

DOI: 10.1021/acsami.6b04219
ACS Appl. Mater. Interfaces 2016, 8, 16752−16760